



TECHNICAL ARTICLE

Effect of Carbon on the Microstructures and Mechanical Properties of a Ni-Based Superalloy with High W Content

Kuo Jiang, Naicheng Sheng, Shijie Sun, Shigang Fan, Jinjiang Yu, Jinguo Li, Lin Yang, Guichen Hou, Yizhou Zhou, and Xiaofeng Sun

Submitted: 2 November 2021 / Revised: 4 February 2022 / Accepted: 28 February 2022 / Published online: 11 April 2022

The microstructures and mechanical properties of experimental Ni-based superalloys K416B with high tungsten (W) content and various carbon (C) contents were studied. The results revealed that C addition led to a decrease in the size and volume fraction of eutectic ($\gamma + \gamma'$) phase. With the increase in C content, the volume fraction and size of MC carbides increased, and an interdendritic network of carbides evolved more prominently. The carbide network occupied most of the interdendritic area and exhibited “dendrite” form. The grain size of the alloy decreased significantly with the increase in C content. The precipitation of α -W is observed in the alloys without C, while M_6C carbides formed when the C content was raised to 0.27 wt.%. No significant change in tensile properties of the alloy when the carbon content increases from 0 to 0.1 wt.%, when the carbon content is increased to 0.27 wt.% the tensile properties of the alloy decrease significantly. With increasing C content, the stress rupture properties increase. Eutectic and grain boundaries are the weak areas in the stress rupture properties process. As the carbon content increases the eutectic content of the alloy decreases, the grain size increases and grain boundaries decreased. Therefore, the stress rupture properties of the alloy improved. The presence of a large amount of primary M_6C reduced the tensile properties of the alloy because the brittle phases in primary M_6C were generated as the carbon content increased, and the primary M_6C was first fractured during tensile testing.

Keywords α -W, carbon, microstructure, mechanical property, Ni-based superalloy, primary M_6C

1. Introduction

Ni-based superalloys are widely used for turbine blades due to their outstanding properties, such as high strength and excellent resistance to oxidation at high temperatures (Ref 1–3). Alloying (with metals like rhenium (Re), ruthenium (Ru), and tungsten (W)) is a widely accepted principle and method to achieve solid solution strengthening of the material (Ref 4, 5). While Re and Ru are rare metals and expensive, the metal W is inexpensive and more effective in improving the temperature-bearing capacity of Ni-based superalloys. Thus, W can replace Re and Ru to a certain extent. The research on Ni-based superalloys with high W content has received extensive attention. At present, a variety of high-W Ni-based superalloys has been developed, such as Mar-M247, K21, and K465, in which the W content is 10 wt.%, with sufficient microstructural stability (Ref 6–9). To further improve the temperature-bearing capacity of the alloy, the W content was further increased to

16 wt.%, and the obtained K416B alloy exhibited good overall mechanical properties and is one of the cast superalloys resisting higher temperatures. The high W content in K416B tends to cause precipitation of W-rich phases (α -W and primary M_6C) during solidification, resulting in a large amount of W consumed in the matrix, which reduces the high-temperature performance of the alloy. K416B alloy contains about 17 wt.% ($\gamma + \gamma'$) eutectic excessive eutectic content would weaken the high-temperature durability of the alloy.

The influence of the variations of elemental content on the microstructure and properties of the alloy is crucial. Carbon is a critical grain-boundary strengthening element in Ni-based superalloys (Ref 10). It has been previously demonstrated that the incipient melting temperature decreased with the addition of C to superalloys, in contrast to other alloy systems (Ref 11, 12). The as-cast microstructures also exhibited a decrease in the amount of eutectic ($\gamma + \gamma'$) structure and an increase in the volume fraction of carbides (MC and M_6C) as the C content increased (Ref 13, 14). The element W is present in the composition of carbides. In particular the W content in M_6C can reach 75 wt.%. Therefore, a variation in the C content of K416B superalloys may cause a change in the W-rich phase (α -W and primary M_6C) and the eutectic phase, thus affecting the high-temperature mechanical properties of the alloy (Ref 15).

In this work, three K416B alloys with C contents of 0 wt.%, 0.1 wt.%, and 0.27 wt.% were prepared. The morphologies of the alloys with different C contents were observed and analyzed to study the effect of C content on the microstructure and properties of Ni-based superalloys and to provide a theoretical basis for the development and application of high-W superalloys.

Kuo Jiang and Lin Yang, School of Materials Science and Engineering, Shenyang University of Technology, Shenyang 110870, People's Republic of China; and Naicheng Sheng, Shijie Sun, Shigang Fan, Jinjiang Yu, Jinguo Li, Guichen Hou, Yizhou Zhou, and Xiaofeng Sun, Shi-changxu Innovation Center For Advanced Materials, Institute of Metal Research, Chinese Academy of Sciences, Shenyang 110016, People's Republic of China. Contact e-mail: ncsheng@imr.ac.cn.

2. Materials and Experiments

The master ingot of K416B alloy used in the present study was prepared by vacuum induction melting. Experimental polycrystalline superalloys with various levels of C were selected. The alloy without C was named alloy C0. The modified alloys with a C content of 0.1 wt.% and 0.27 wt.% were named alloy C1 and alloy C2, respectively. Chemical compositions of the samples were analyzed using spark-emission spectroscopy (Zetium, Malvern Panalytical) and a carbon-sulfur analyzer (HCS-500, Yima). The chemical composition (wt.%) of the three K416B superalloys is shown in Table 1.

K416B specimen of a diameter of 8 mm and the height of 5 mm was cut from the middle of the sample. After mechanical grinding and polishing, optical microscopy (OM) (Stemi 508, Zeiss) was used to examine the grain structure of the specimens. To reveal the microstructures, samples were etched with 20 g CuSO₄ + 5 mL H₂SO₄ + 100 mL HCl + 80 mL H₂O before examination by scanning electron microscopy (SEM) (MIRA, Tescan, and S-3400N, Hitachi). Secondary electron mode was used for analyzing the morphology of the eutectic ($\gamma + \gamma'$). Backscattered electron (BSE) imaging was used to analyze the microstructures of carbides and α -W. The composition of various precipitated phases was determined by energy-dispersive x-ray spectroscopy (EDS) and electron probe microanalysis (EPMA). The W-rich phases in C0 and C2 alloys were identified using electron backscatter diffraction (EBSD) as α -W and primary M₆C. The deformation mechanisms during the deformation of the alloy were examined using transmission electron microscope (TEM). Using the characteristics of eutectic tissue and different color of the carbide, the color was differentiated from the surrounding tissue by Photoshop software.

The area fractions of carbides, eutectic ($\gamma + \gamma'$), carbide, and secondary dendrites were analyzed using Image-Pro software. To obtain the phase transition temperatures, differential scanning calorimetry (DSC) was performed with a thermal

analyzer (STA 449 F3, Netzsch). The specimens used for DSC were cut from the master ingot with a size of 3 mm diameter and 2 mm height. It should be noted that the DSC experiments were conducted in a high-purity Ar atmosphere to avoid oxidation. Since the phase transformation occurred in the temperature range of 800–1450 °C, only data within this interval were analyzed.

Specimens with a diameter of 5 mm and a gage length of 30 mm were machined from the bars to study the tensile behavior. The alloy bar was processed into samples for room-temperature tensile tests, which were conducted with an electronic universal testing machine (INSTRON, 5982) to assess yield strength, tensile strength, post-fracture elongation, and fracture shrinkage of alloy test bars of different C content.

Threaded stress rupture properties specimens were machined from the bars, the specimens have a diameter of 5 mm and a gauge length of 25 mm. The effect of C content on stress rupture properties was examined. Equiaxial-crystal specimen bars of the alloys were mechanically processed into stress rupture property specimens. Specimens with different C contents were subjected to stress rupture testing at 975 °C and 235 MPa to assess the durability life of alloys in relation to their C content under these conditions and to investigate the effect of C content on the stress rupture properties at high temperature.

3. Results

3.1 Microstructure

3.1.1 Grain Structures. The grain morphologies of the alloys C0, C1, and C2 were observed via OM and are presented in Fig. 1. From Fig. 1, it can be seen that the type of the alloy is equiaxed, and the color of the grains is different due to the different grain orientation. Indicating that the grain size

Table 1 Chemical compositions of the experimental K416B alloys (wt.%)

| Alloy | C | Cr | Co | Al | W | Ti | Nb | Hf | B + Zr | Ni |
|-------|------|-----|-----|------|------|-----|-----|-----|--------|------|
| C0 | 0 | 5.1 | 7.8 | 5.85 | 15.7 | 0.8 | 1.8 | 0.9 | 0.03 | Bal. |
| C1 | 0.1 | 5.1 | 7.8 | 5.85 | 15.7 | 0.8 | 1.8 | 0.9 | 0.03 | Bal. |
| C2 | 0.27 | 5.1 | 7.8 | 5.85 | 15.7 | 0.8 | 1.8 | 0.9 | 0.03 | Bal. |

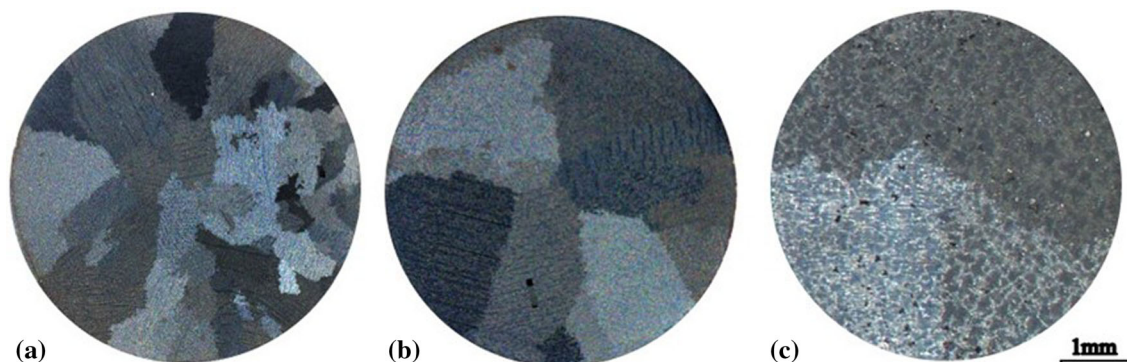


Fig. 1 OM images of the alloys with different C content at low magnification: (a) 0 wt.% C, (b) 0.1 wt.% C, (c) 0.27 wt.% C

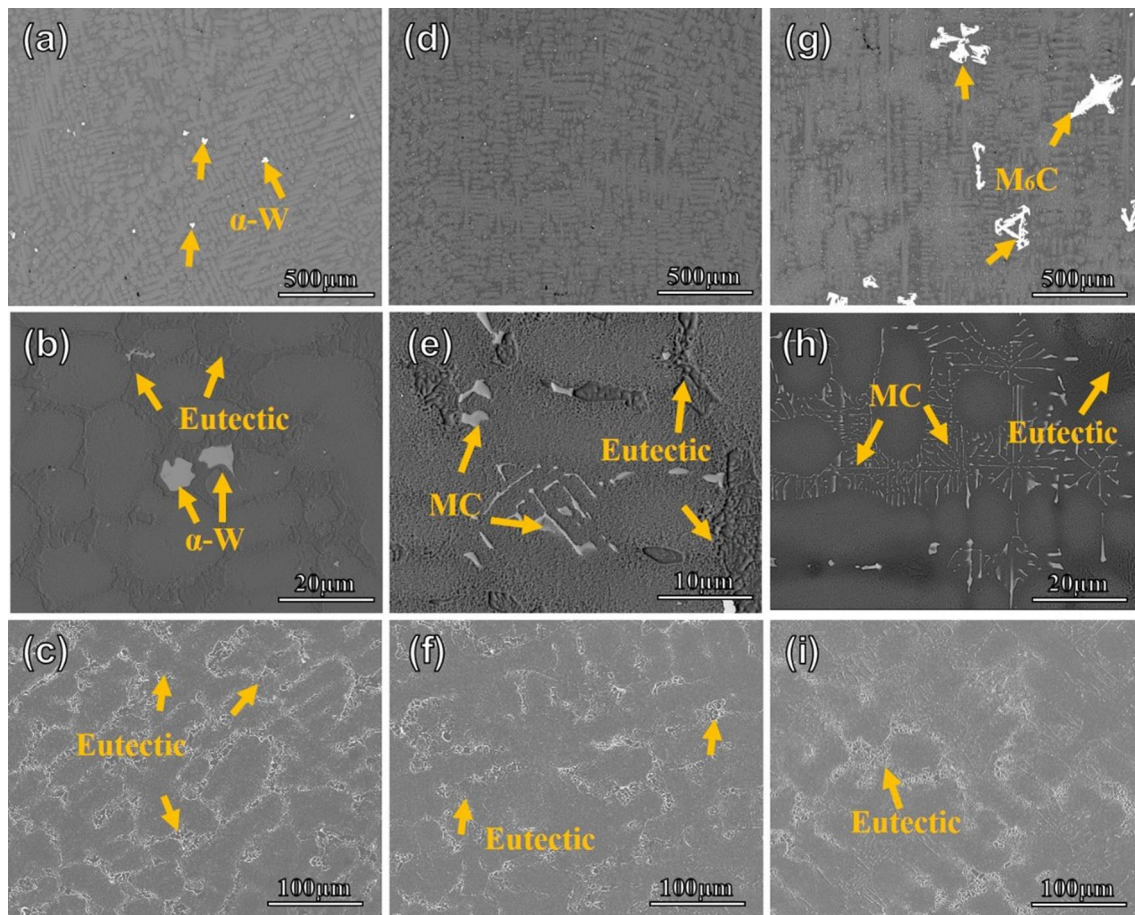


Fig. 2 SEM images showing typical microstructures of K416B alloys with various C contents: (a-c) 0 wt.% C, (d-f) 0.1 wt.% C, (g-i) 0.27 wt.% C

increased significantly as the C content.

3.1.2 Eutectic and MC Carbides. The interdendritic region contained many irregularly dispersed eutectic ($\gamma + \gamma'$) regions as shown in Fig. 2. The amount of eutectic ($\gamma + \gamma'$) phase decreased as the C content increased in the alloy. Quantitative calculations revealed that the fraction of the eutectic area decreased significantly with the increase in C content, and the average cross-sectional area decreased from 22.64 to 13.67%, as shown in Fig. 3. The result is in agreement with the research result reported by Wasson et al. (Ref 14).

The bright MC-type carbide phases indicated in the BSE images in Fig. 2 were mostly distributed in interdendritic positions. The micrographs of the alloy C0 showed large pools of eutectic in Fig. 2(a), (b) and (c). The carbides in alloy C1 were mainly present in the form of needles and Chinese script-type shape. All MC-type carbides in alloy C2 exhibited a Chinese script-type shape. As the C content increased, an interdendritic network of carbides evolved more prominently, as evident from Fig. 4(b), (e) and (h). Similar results were reported in the previous literature. The carbide network occupied most of the interdendritic area and exhibited “dendrite” form. Quantitative calculations concluded that the average fraction of MC areas increased significantly with the increase in C content, and, as shown in Fig. 3, the average cross-sectional areas increased from 0% in alloy C0 over 1.3% in alloy C1 to 6.1% in alloy C2.

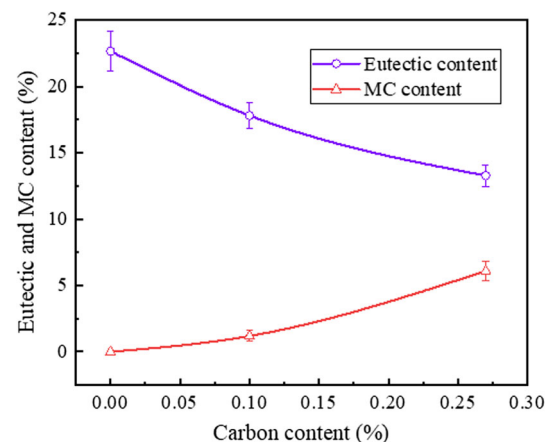


Fig. 3 Area-based eutectic and MC carbide content in the alloys with different C contents

The dendrite morphology of the three alloys is also shown in Fig. 2. The dendrite morphology did not change significantly with the increase in C content. The secondary dendrite arm spacing (SDAS) of the alloys remained basically constant as the C content increased. Since the SDAS is considered as a characterization parameter of the cooling rate during the solidification of the casting (Ref 16, 17), it is confirmed that

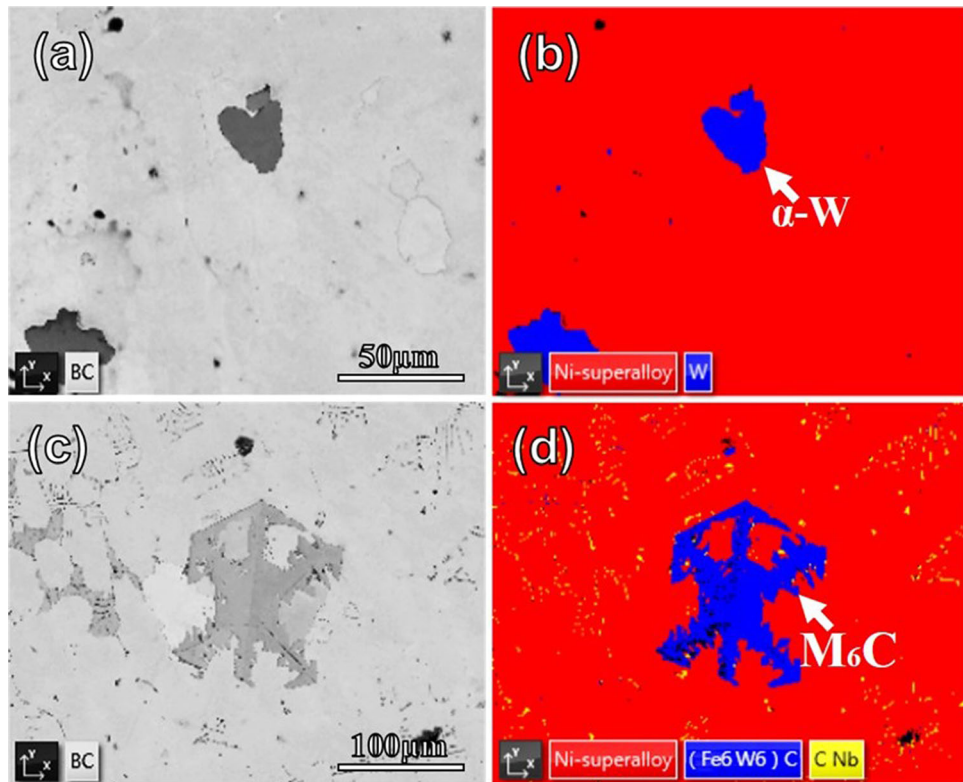


Fig. 4 EBSD showing the morphology of W-rich phases: (a, b) α -W, (c, d) primary M_6C

the almost constant spacing inferred that the cooling rates of the three alloys were nearly the same.

3.1.3 W-rich Phases (α -W and M_6C). The typical morphology of the W-rich phase is shown in Fig. 4(a) for alloy C0 and in Fig. 4(c) for alloy C2. The two phases were identified as α -W and primary M_6C by EBSD analysis, and the results are shown in Fig. 4(b) and (d). The α -W phase precipitated in alloy C0 exhibited rosette-type shapes with sizes of about 25 μm and was surrounded by eutectic ($\gamma + \gamma'$) phase in a uniform distribution. The EDS analysis results are shown in Table 2. The precipitated phase mainly consists of W in a weight fraction of about 94 wt.%, thus confirming that the precipitated phase is α -W. In Fig. 4(d), primary M_6C carbides are present in alloy C2 in regular angular and anchor shapes. This carbide often coexists with eutectic ($\gamma + \gamma'$) and possesses sizes of about 100 μm . The composition of M_6C carbides determined by EDS is listed in Table 1 and includes W, Ni, C, Co, and Cr. The W content of 72 wt.% implies that the precipitated phase is primary M_6C .

3.2 DSC and EPMA Analysis

Figure 5 shows the DSC cooling curves of the different alloys in the range of 1450–800 $^{\circ}C$, from which the main phase transformation temperatures were determined. In alloy C0, γ matrix crystallized from the liquid at 1381 $^{\circ}C$, the eutectic ($\gamma + \gamma'$) formed at 1285 $^{\circ}C$, and γ' phase formed at 1211 $^{\circ}C$. In the cooling curve of alloy C1, due to the addition of carbon, the formation temperature of MC carbides can be clearly seen. The following five phase transformation temperatures were observed for C1: γ matrix crystallized from the liquid at 1372 $^{\circ}C$, MC carbides precipitated at 1325 $^{\circ}C$, the eutectic ($\gamma + \gamma'$) formation occurred at 1281 $^{\circ}C$, and γ' phase formed

Table 2 Compositions of typical precipitates analyzed by EDS (mass fraction, wt.%)

| Phases | C | W | Co | Cr | Ni |
|-------------|------|-------|------|------|------|
| M_6C | 5.86 | 72.02 | 3.77 | 2.93 | Bal. |
| α -W | 0 | 94.62 | 0 | 0 | Bal. |

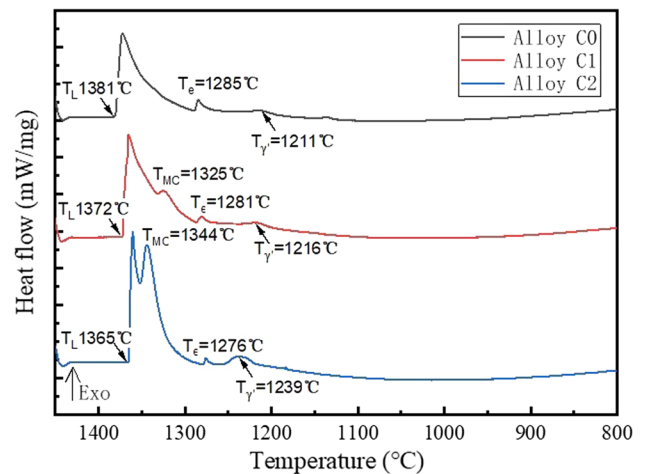


Fig. 5 DSC cooling curves of the alloys with various C contents

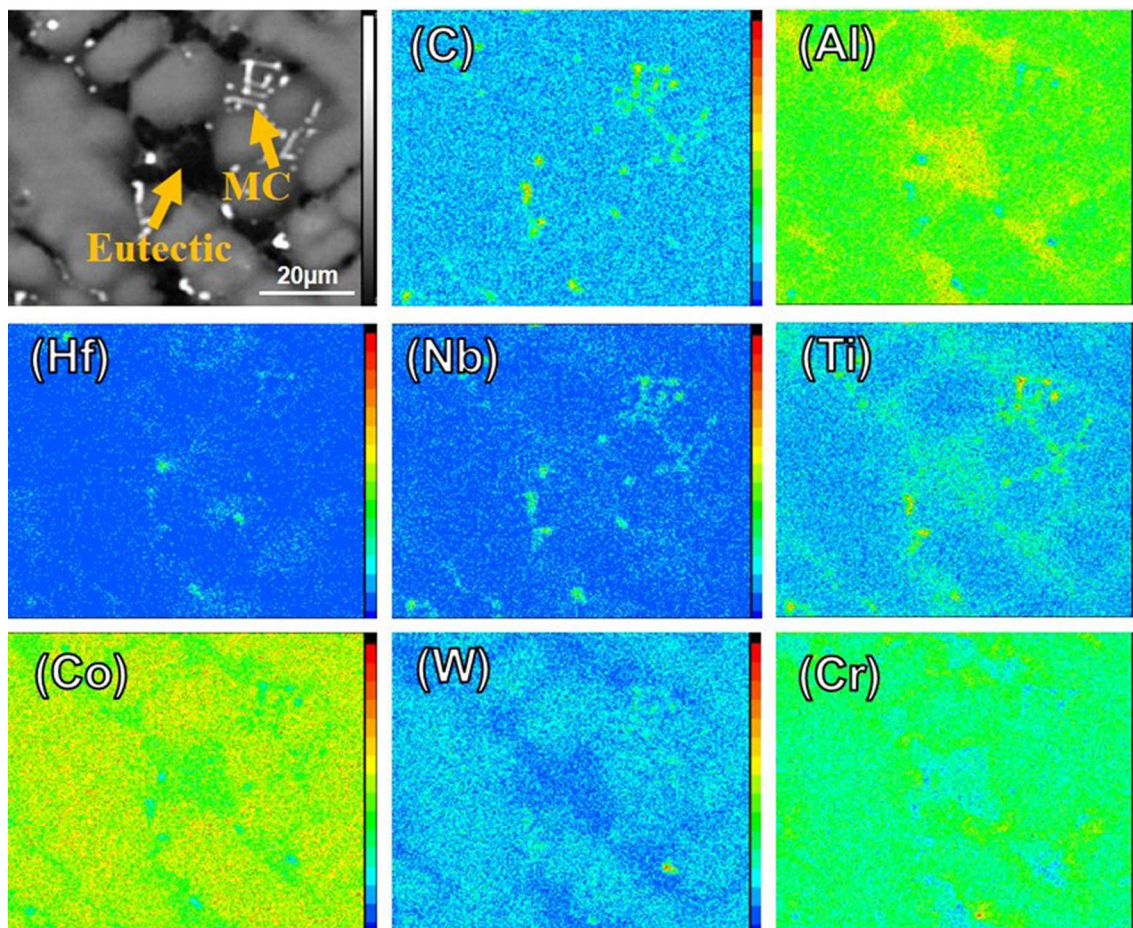


Fig. 6 Distribution of different elements in alloy C1 with 0.1 wt.% C content

at 1216 °C. The carbon content in alloy C2 was more than that in alloy C1, and the obvious MC formation temperature can be seen in the C2 cooling curve. Five phase transformation temperatures were determined: γ matrix crystallized from the liquid at 1365 °C, MC carbides precipitated at 1344 °C, the eutectic ($\gamma + \gamma'$) formed at 1276 °C, and γ' phase formed at 1239 °C. According to Fig. 5, from C0 to C1 to C2, the temperature of γ matrix crystallization from the liquid and eutectic ($\gamma + \gamma'$) formation significantly decreased, while γ' phase formation temperature increased. The MC formation temperature increased from C1 to C2. Based on the analysis of the DSC cooling curves, the phase transformation process, starting with the liquid phase, can be described as: $L \rightarrow \gamma$; $L \rightarrow \gamma + MC$; $L \rightarrow \text{eutectic } (\gamma' + \gamma')$; $\gamma \rightarrow \gamma'$.

According to the EPMA maps of the sample alloy C1 (Fig. 6), the segregation behavior of different elements in different phases can be analyzed. W and Co elements were mainly segregated in the region of the dendrites, while Al, Ti, and Nb were segregated in the interdendritic region. The carbides were composed of C, Ti, Nb, W, and Hf, and the eutectics were composed of Al, Ti, and Nb, as evident from Fig. 6.

3.3 Mechanical Properties

3.3.1 Tensile Tests. The tensile properties of K416B alloy with different carbon contents are shown in Fig. 7. As the carbon content increased from 0 to 0.1-0.27%, the yield strength of the alloy decreased slightly from 910 to 915-745

MPa. In addition, the elongation of the alloy was 4% when the carbon content was 0 and 0.1%. When the carbon content increased to 0.27%, the plasticity of the alloy dropped sharply and the elongation of the alloy dropped to 0.4%.

The microstructure of the break region of the alloys after room-temperature tensile fracture is shown in Fig. 8. It can be seen that most of the cracks in alloys C0 and C1 sprouted at the eutectic edge, and the cracks in C2 alloy sprouted at the primary M_6C . The primary M_6C was present in the alloy as a brittle phase.

According to Fig. 8(a) and (b), the cracks were mainly generated at the eutectic ($\gamma + \gamma'$) and expanded along the eutectic edge, as marked by the arrows in the two figures. In Fig. 8(c) and (d), microcracks were generated around the carbide and extended along the eutectic edges. The carbide was mainly present in the interdendritic or grain boundaries, suggesting that the interdendritic as well as the grain boundary regions were the main areas where the cracking source of the alloy was generated. One can conclude that stress concentration around the carbide occurred and led to microcracking at the carbide. With the increase in alloy strain, stress concentration occurred at the crack tip and expanded rapidly, leading to fracture of the alloy.

As observed in Fig. 8(e) and (f), the primary M_6C phase is a brittle phase. The cracks were first generated at the primary M_6C , and long cracks were formed by the convergence of small cracks. Therefore, during room-temperature stretching, stress concentration first occurred around M_6C , and as the alloy strain

increased, multiple microcracks rapidly expanded and converged, leading to the fracture of the alloy (Ref 18).

The TEM image of C0 alloy after room temperature tensile fracture is shown in Fig. 9(a). After room temperature tensile test, a large number of stacking faults were observed in the alloy. Under external forces, deformation dislocations can form dislocation rings in the matrix with $\langle 110 \rangle$ dislocation shear γ' phase. The floral precipitation phase was also found in the specimen, which was identified by diffraction spotting as α -W, in agreement with the above EBSD test results.

TEM images of alloy C1 after room temperature tensile fracture are shown in Fig. 9(c). It can be seen that the number of dislocations increased significantly, the dislocations in the matrix opened and proliferated, and intersected and entangled with other dislocations in the matrix, showing obvious dislocation channels in the TEM photograph. In areas of severe deformation, these dislocation entanglements caused local stress concentrations. The dislocation lines were orientated differently, as seen in Fig. 9, which indicates that multiple slip systems were initiated. TEM images of C2 alloy after room temperature tensile fracture are shown in Fig. 9(d). It can be

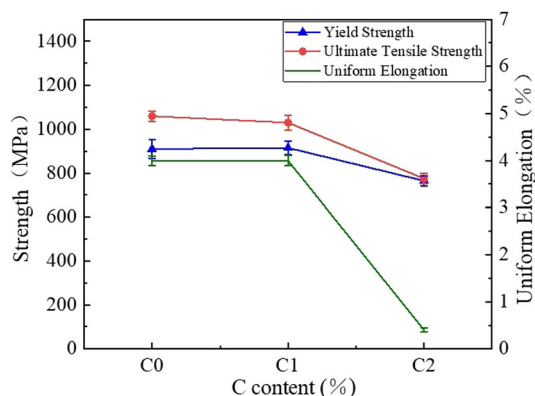


Fig. 7 Room-temperature tensile data of alloys C0, C1, and C2

seen that there were a large number of individual dislocations and dislocation pairs in the alloy where the stacking fault disappeared. Moreover, a significant reduction in stacking fault and dislocation entanglement was observed, which is detrimental to the tensile properties of the alloy.

3.3.2 Stress Rupture Properties. Table 3 shows the rupture life curves of the alloys with different carbon contents. The durability of the alloy increased significantly with the increase in C content, and the C2 alloy with a C content of 0.27 wt.% demonstrated the longest durability under the applied conditions of 975 °C and 235 MPa.

The morphologies of crack initiation and propagation of the C0 alloy after stress rupture property test at 975 °C and 235 MPa are shown in Fig. 10(a) and (b). The cracking of the alloy during the stress rupture property test occurred mainly at the eutectic edges and holes at the grain boundaries and extended along the grain boundaries. After alloy C0 was fractured at 975 °C and 235 MPa, the morphology of the near-fracture area of the fractured test bar was observed. The obtained crack extension morphology is shown in Fig. 10(a), which indicates that cracks in these alloys grew along grain boundaries until fracture.

The morphologies of crack initiation and propagation of the C1 alloy after stress rupture property test at 975 °C and 235 MPa are shown in Fig. 10(c) and (d). The cracks sprouted mainly at the carbides and holes at the eutectic edges and extended along the eutectic edges at the grain boundaries during the endurance test of the alloy. When the grain boundary at the location of the crack source exhibited a curved shape, cracks connected with each other facilitated the formation of macroscopic cracks. These observations indicate that eutectic and grain boundaries were the main crack sources.

The cracks in the near-fracture region of alloy C2 after fracture at 975 °C and 235 MPa are shown in Fig. 10(e) and (f). The cracks were mainly generated by M_6C fracture during persistent fracture of the alloy and extended along the surrounding MC carbide of Chinese-script shapes. Due to its large grain size with few grain boundaries and low eutectic content, no eutectic and grain boundaries were observed around

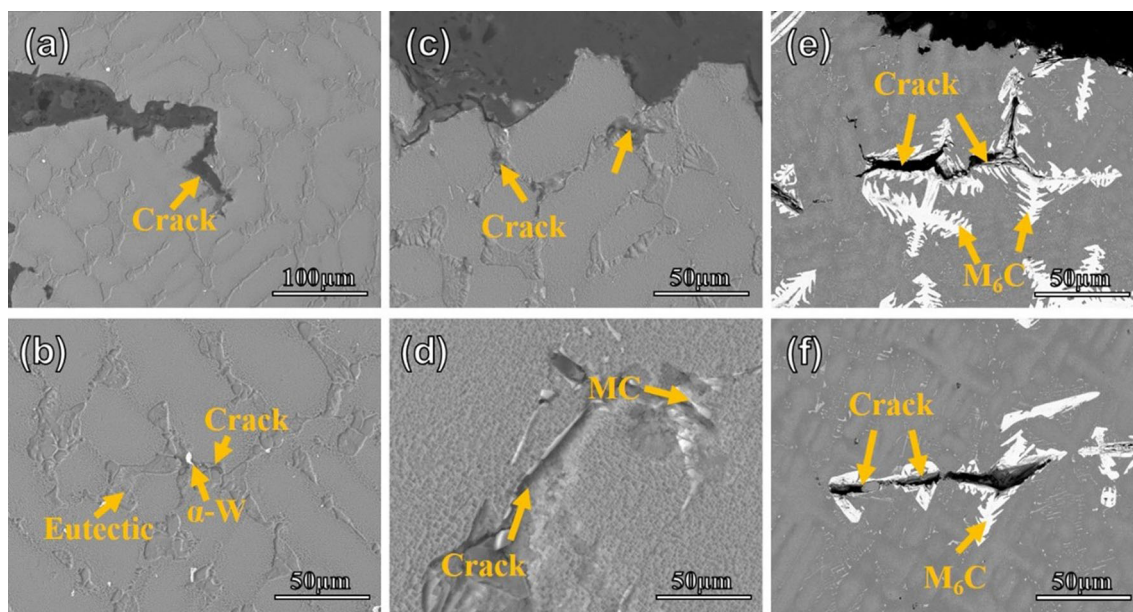


Fig. 8 SEM images of the longitudinal section of superalloys with various C content after tensile fracture: (a, b) 0 wt.% C, (c, d) 0.1 wt.% C, (e, f) 0.27 wt.% C

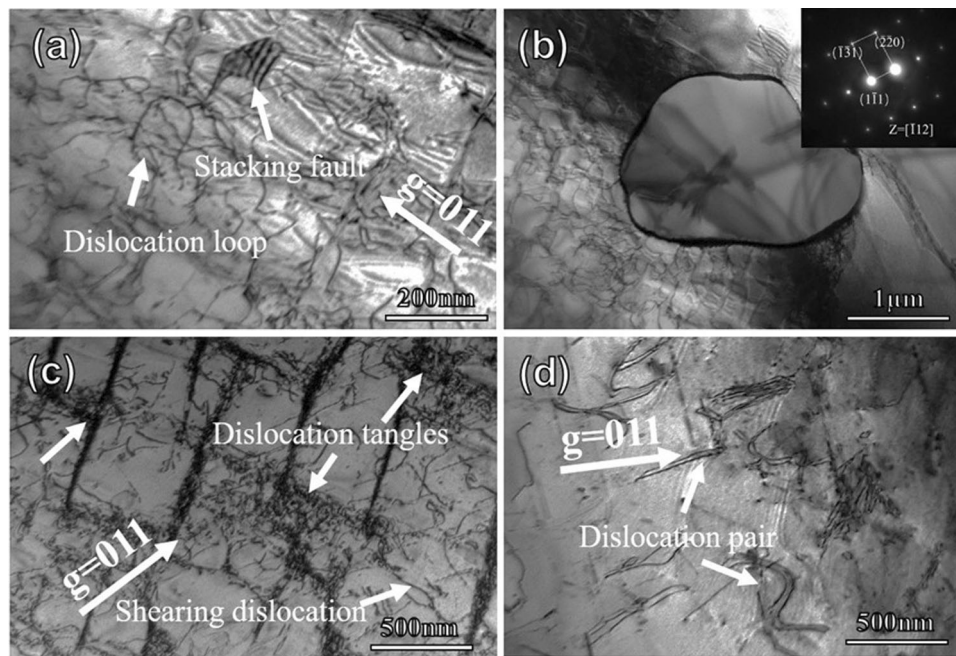


Fig. 9 TEM images after room-temperature tensile fracture of alloys with various C contents: (a, b) 0 wt.% C, (c) 0.1 wt.% C, (d) 0.27 wt.% C

Table 3 Stress rupture properties of superalloys with various C contents at 975 °C/235 MPa

| Carbon content, wt.% | 0 | 0.1 | 0.27 |
|----------------------|------|------|------|
| Rupture life (h) | 16.8 | 32.4 | 45 |

the crack. The cracking of the alloy during persistent testing is mainly generated by the fracture of M_6C and extended along the surrounding carbide.

The microstructures of the different alloys after stress rupture property test at 975 °C/235 MPa are shown in Fig. 11. During deformation, dislocations move in the octahedral slip system of the γ matrix and form irregular dislocation networks. Figure 11(a) and (b) shows that the dislocation network in C1 alloy has regular parallelogram shape. This parallelogram shape dislocation network can lock the dislocations around the dislocation network, making it difficult to cut into the γ' phase and improving the properties of the alloy. In Fig. 11(c) it can be seen that the dislocations in the C2 alloy move mainly bypass, because the increase in carbon content creates a large number of fine diffuse MC carbides. Dislocations need to travel longer distances and consume more of their own energy, resulting in improved mechanical properties of the alloy. However, the most important factors affecting the stress rupture properties of the alloy are the eutectic content and variation in grain size which will be explained detail in the discussion section.

4. Discussions

4.1 Effect of Carbon on Microstructures

4.1.1 Grain Structures. Figure. 1 shows that the grain size of the alloys increases significantly with increase in C content, and the grain boundaries decrease significantly from

about 1 mm to 5 mm. Figure. 4 presents that the SDAS is approximately the same for all three alloys. Therefore, it can be inferred that the variation in grain size of the alloys does not depend directly on the solidification rate (Ref 19, 20). The initial solidification temperatures were determined by DSC as 1381 °C for C0, 1372 °C for C1, and 1365 °C for C2 (Fig. 5). The casting temperature of all three alloys is 1550 °C. Due to the increase in the difference between the casting temperature and the initial solidification temperature, a large amount of impurities melted. Consequently, so that the number of non-uniformly shaped cores decreased resulting in a morphology closer to the uniformly shaped core state. As previously reported, the relationship between the critical nucleation radius (r^*) and the initial solidification temperature (T_m) is the following (Ref 21, 22):

$$r^* = \frac{2\sigma \cdot T_m}{L_m \cdot (T_m - T)} \quad (\text{Eq 1})$$

where r^* is the critical nucleation radius, σ is the specific surface energy, L_m is the heat of melting, T_m is the initial solidification temperature, and T is the actual liquid-phase temperature. Since processing and main alloy composition are the same for all three alloys, it can be assumed that σ , L_m , and T are constant, and the critical nucleation radius r^* increases as the initial solidification temperature T_m decreases. Therefore, it can be inferred that the initial solidification temperature of the alloy decreases as the content of C increases, causing an increase in the critical nucleation radius of the alloy, which is not conducive to nucleation during solidification, resulting in an increase in the grain size of the alloy.

4.1.2 Eutectic and Carbides. According to the precipitation temperatures determined during DSC investigations, MC carbides precipitate at an earlier stage of solidification than the eutectic ($\gamma + \gamma'$) (Ref 23). It can be concluded that MC carbides and eutectic constitute the entire solidification products of interdendritic liquids, but the carbide forms earlier than

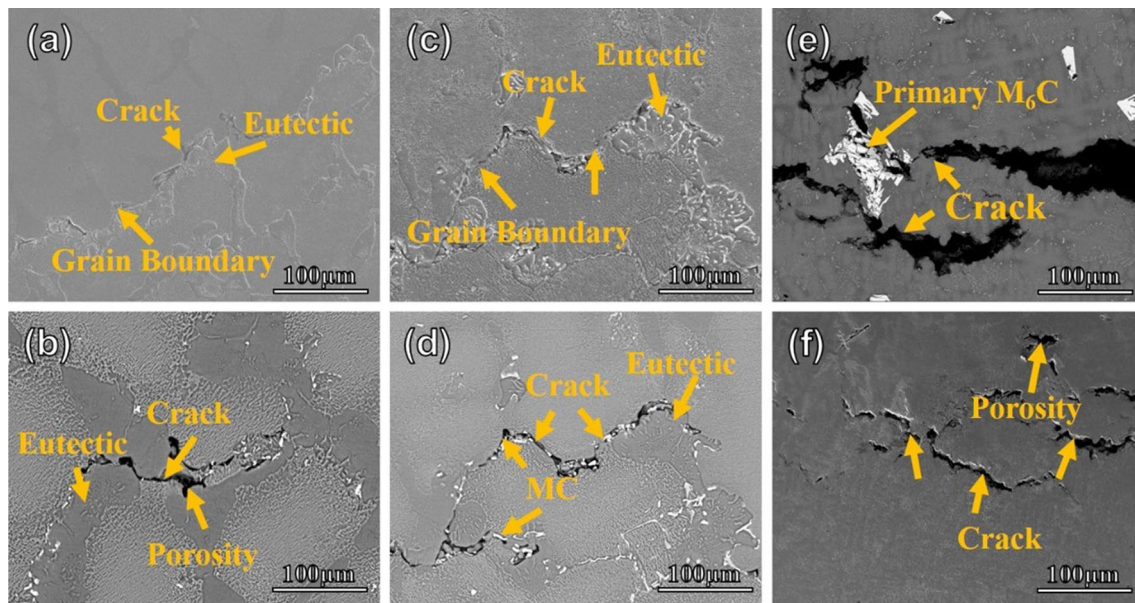


Fig. 10 SEM images of cracks in superalloys with different C contents (975 °C/235 MPa): (a, b) 0 wt.% C, (c, d) 0.1 wt.% C, (e, f) 0.27 wt.% C

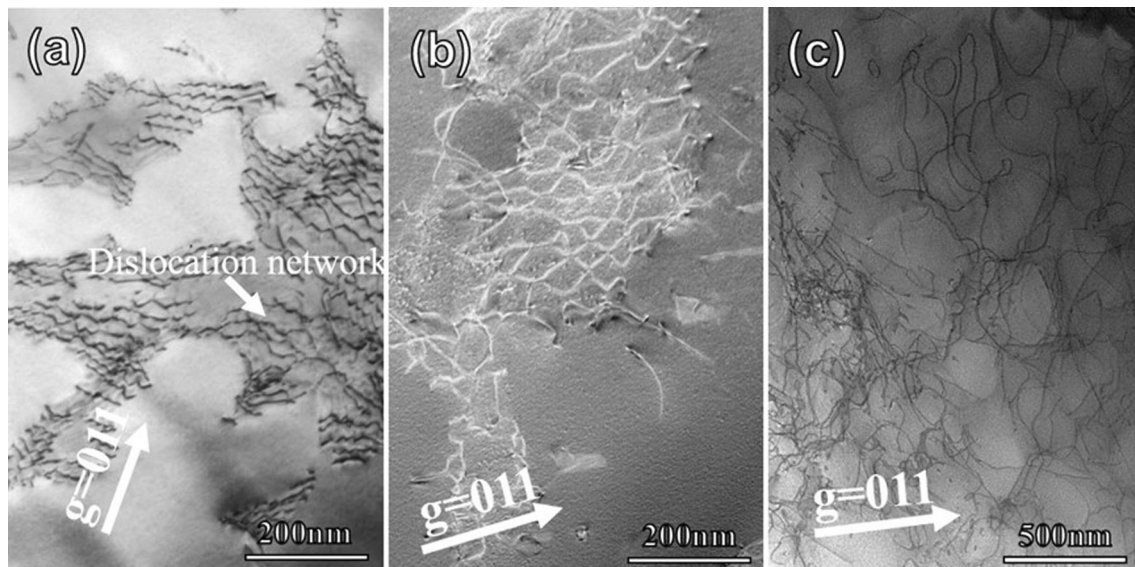


Fig. 11 TEM images after stress rupture property test with various C contents: (a) 0 wt.% C, (b) 0.1 wt.% C, (c) 0.27 wt.% C

the eutectic. EPMA analysis indicates that MC carbide and eutectic are both rich in Ti and Nb (Fig. 6). Ti and Nb have been previously identified as the MC carbide-forming elements in Ni-based superalloys. Since the MC carbide consumes a part of Ti and Nb in the interdendritic regions, the remaining amounts of these two elements are reduced in these regions, whose compositions consequently deviate from the composition for eutectic formation (Ref 12, 24). Since the formation of carbide consumes a large amount of eutectic-forming elements Nb and Ti, the content of eutectic is reduced.

As shown in Fig. 2, with the increase in carbon content, the distribution of carbides changes. Most of the MC carbides in the C1 alloy are distributed between the dendrites in Chinese script-type shape or small rods. With the increase in carbon

content in C2, the area fraction of MC carbides increases, and a large number of MC carbides combine together to appear as “dendrites”. The solidification process is shown in Fig. 12(a) and (b), where the primary dendritic arm grows first at the beginning of solidification, then the secondary dendritic arm precipitates from the primary dendritic arm. As solidification proceeds, the primary and secondary dendritic arms continue to grow, and at the end of solidification, the adjacent secondary dendritic arms contact each other, as shown in Fig. 12(b). The DSC results in Fig. 5 show that the MC carbide formation temperature is 1325 °C in C1 and 1344 °C in C2. The higher C content in C2 leads to a higher MC precipitation temperature compared to C1.

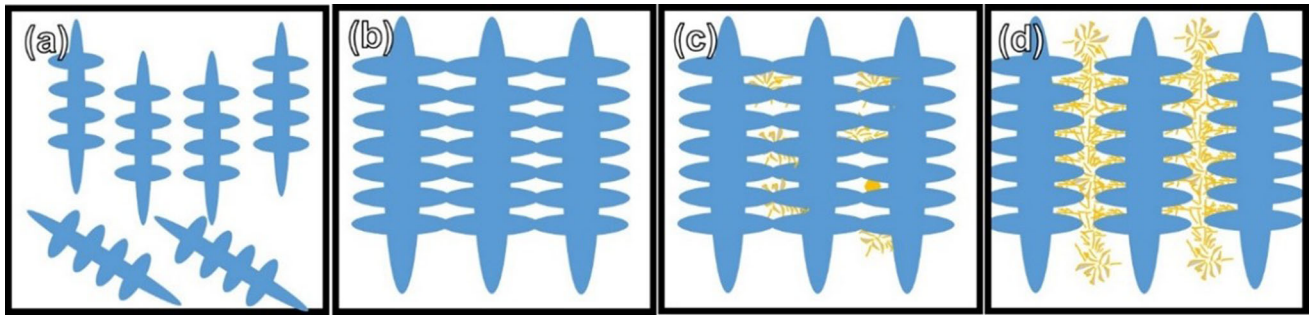


Fig. 12 Dendrite growth during solidification of alloys with different carbon contents: (a, b) 0 wt.% C, (c) 0.1 wt.% C, (d) 0.27 wt.% C

In C1 alloy, MC carbides are produced after the adjacent secondary dendrite arms are joined, as shown in Fig. 12(c). The MC carbide precipitation temperature in alloy C2 is higher and the MC carbide starts to precipitate and grow before the secondary dendrite arms are connected during the dendrite growth process (Ref 25, 26). This results in the formation of a “dendritic” carbide network between the dendrites, as shown in Fig. 12(d).

4.1.3 W-rich Phases (α -W and M_6C). The morphological observation of the alloys with different C contents showed that the amount of α -W phase was greatly reduced when the C content was increased from 0 to 0.27 wt.%, as shown in Fig. 2. Since W is contained in MC carbides, W is consumed with increase in C content via MC formation in the dendrites. Since the precipitation temperature of α -W is high, the $L \rightarrow \alpha$ -W transition occurs first if α -W phase is precipitated during the liquid-solid transition, and the driving force of α -W phase precipitation is the free energy change caused by W-atom segregation. Therefore, it can be assumed that, with decrease in free energy change caused by W-atom deflection in the liquid phase, the occurrence of W-atom deflection during solidification and the precipitation of α -W phase is promoted.

$$\Delta G_{\text{sur}} = \Delta H_{\text{mix}}(X_s - X_b) \quad (\text{Eq 2})$$

where ΔH_{mix} is the enthalpy of mixing of W in Ni, and X_s and X_b are the element fractions in the α -W phase and the yard of the alloy, respectively. The W content in the α -W phase can be considered more than 90 wt.% according to the compositional characteristics of the α -W phase (Ref 21), and to over Miedema's hemispheric empirical model for the calculation of the mixing culmination of W in Ni.

$$\Delta H_{\text{mix}} = 4.18f(x_s, V^a) \times \left[-(\Delta\phi^*)^2 + \frac{Q}{P} \left(\Delta n_{\text{ws}}^{1/3} \right)^2 - \frac{R}{P} \right] \quad (\text{Eq 3})$$

where Q/P and R/P are correction factors, Δn_{ws} is the Wigner–Seitz atomic cell boundary of the element (Ref 22), ϕ^* is the correction function of the element, and x_s and V_a denote the molar fraction and molar volume of the element. With the increase in C content, a certain amount of W is consumed in the process of carbide generation, which inhibits W polarization and causes the increase in surface free energy. Based on the thermodynamic analysis, the increase in C content can inhibit the $L \rightarrow \alpha$ -W transition.

Primary M_6C phase mostly exists in high-W and high-C alloys, and its composition is relatively stable with W content of about 75 wt.% and small amounts of C, Co, and Cr. Primary

M_6C is a brittle phase, and the hardness value of primary M_6C under Vickers hardness test is in the range of 1.48×10^4 – 1.68×10^4 MPa. Rapid cooling can inhibit the formation of M_6C (Ref 27). Due to the high W content of primary M_6C , it is have high melting point.

4.2 Effect of Carbon Content on Mechanical Properties

4.2.1 Tensile Tests. As the carbon content increases, the density of deformation dislocations in the alloy gradually decreases, and only a small number of dislocations in the C2 alloy slip and bow out in the matrix to form dislocations of different sizes. This indicates that the dislocations cross the γ' phase by an Orowan mechanism, while the $\langle 110 \rangle$ superdislocations that cut into the γ' phase can decompose with increase in tensile stress to form a dislocation group of incomplete dislocations+ stacking fault, as shown in Fig. 9(b). The formation of high-density dislocations in the matrix of C0 and C1 alloys produces a deformation strengthening effect. This is one of the reasons for the high yield and tensile strength of the alloy. During room temperature stretching of C0 and C1 alloys, deformation dislocations are activated mainly in the γ matrix. As the number of deformation dislocations in the γ matrix increases, stress concentration is generated at the γ/γ' inter face plugging. This results in dislocations cutting into the γ' phase, which can effectively release the concentrated stress and make the stretching continuous. As the number of dislocations cutting into the γ' phase increases, larger plastic deformation occurs, which is one of the main reasons why C0 and C1 have higher elongation than C2. A few dislocations in C2 alloy effectively release some of the stress concentrations generated by dislocations. Thus, the alloy strength decreases significantly with a large tensile strain rate. As a result, the alloy flow stress is much higher than the effective release stress value of the alloy. When the accumulated rheological stress is higher than the alloy yield strength, the alloy fractures, which is one of the main reasons for the decreased elongation of the alloy.

As the carbon content increases to 0.27 wt.%, the tensile properties of the alloy decrease significantly. According to Fig. 8(a) and (b), the cracks in alloy C0 are mainly formed at the eutectic edges and expand around these edges into large cracks until fracture. As observed in Fig. 8(c) and (d), stress concentrations first occur around the carbide at the eutectic edge and lead to microcracking at the carbide; as the alloy strain increases, stress concentrations occur at the crack tip and expand immediately leading to fracture of the alloy. A large amount of primary M_6C , which is known to form a brittle phase, is generated in the C2 alloy. According to Fig. 8(e) and

(f), stress concentrations are first generated around M_6C , and cracks are first generated at the primary M_6C (Ref 28); as the alloy strain increases, multiple microcracks expand rapidly and converge, resulting in alloy fracture. Therefore, the main reason for the decrease in tensile properties of the alloy with increase in C content is the precipitation of a large amount of brittle primary M_6C . The uniform elongation of C0 and C1 is slightly higher than that of C2 alloy because the large amount of M_6C phase in the C2 alloy also causes stress concentrations that significantly reduce the uniform elongation of the alloy.

4.2.2 Stress Rupture Properties. The main reason for the increase in dislocation density with increase in carbon content is that the increase in carbide content in the alloy impedes dislocation movement and leads to dislocation plugging. The stress rupture properties of the alloy increase with increase in C content. As evident from Fig. 10(a), (b), (c), and (d), the microcracks of C0 and C1 alloys mainly occur at the α -W or MC carbide phase around the eutectic and extend along the eutectic edge with the fracture location at the grain boundary, while the cracks of C2 alloy mainly occur at the primary M_6C phase and extend along the Chinese script-shaped MC carbide. These observations indicate that the weak areas of the alloy in the stress rupture tests are mainly the eutectic and grain boundaries. C is added to the alloy as a grain-boundary strengthening element (Ref 29). As the C content increases, the eutectic area fraction decreases, reducing the number of locations for microcracking in the alloy. Since the grain size of the alloy increases with increase in C content, the number and area of grain boundaries are reduced, impeding the expansion of cracks. Therefore, stress rupture properties improve with increase in C content of the alloys.

5. Conclusion

In this paper, small amounts of C were added to high-W Ni-based superalloys. The main conclusions of the present investigation are the following.

1. The presence of α -W was observed in alloy without C, while M_6C precipitated in C2 with increase in C content.
2. With the increase in C content, the grain size increased obviously. Increase in C addition caused an increase in MC carbide content and a decrease in eutectic content.
3. As the C content increased, the stress rupture properties increased. There was no significant change in tensile properties as the carbon content increased from 0 to 0.1, while tensile properties decreased as C content increased to 0.27.

Author Contributions

KJ contributed to conceptualization, data curation, and writing-original draft preparation. NS contributed to conceptualization, methodology, funding acquisition, and project administration. SS contributed to methodology and writing-reviewing. SF contributed to software. JY contributed to data curation and validation. JL contributed to technical guidance and validation. LY contributed to software, validation, and writing-reviewing. YZ contributed to

technical guidance and software. XS and GH contributed to conceptualization and methodology.

Conflict of interest

The authors report no declarations of interest.

References

1. Z. Liang, G. Zhang, T.L. Lee, M.J. Gorley, W. Yue, C. Xiao, and L. Zhou, The Effects of Ta on the Stress Rupture Properties and Microstructural Stability of a Novel Ni-Base Superalloy for Land-Based High Temperature Applications, *Mater. Des.*, 2014, **61**, p 61–69
2. H. Zhao, W. Feng, and T. Zhou, Distribution of Primary M_6C Carbide in Large Nickel-Based Superalloy Casting, *Foundry Technol.*, 2017, **38**, p 1288–1291
3. S. Behera, M.K. Dash, N.K. Kumar, R. Mitra, and G.A. Rao, Microstructure and High-Temperature Tensile Behavior of Ni-Based Superalloy EP741NP for Aerospace Applications, *J. Mater. Eng. Perform.*, 2021, **30**, p 5834–5844
4. A. Heckl, S. Neumeier, M. Goken, and R.F. Singer, The Effect of Re and Ru on γ/γ' Microstructure, γ -Solid Solution Strengthening and Creep Strength in Nickel-Base Superalloys, *Mater. Sci. Eng. A*, 2011, **528**, p 3435–3444
5. S.J. Sun, N.C. Sheng, S.G. Fan, Y.Z. Ma, X. Cao, and Z.R. Sang, Abnormal Feather-Like Grains Induced by the Tin-Wall Effect in a Polycrystalline Nickel-Based Superalloy, *J. Alloys Compd.*, 2022, **901**, p 163581
6. D. Peng, R.L. Brodin, and H. Moverare, Microstructure and Mechanical Properties of Inconel 718 Produced by Selective Laser Melting: Sample Orientation Dependence and Effects of Post Heat Treatments, *Mater. Sci. Eng. A*, 2010, **713**, p 294–306
7. X.F. Yuan, J.X. Song, Y.R. Zheng, Q. Huang, K. Yagi, C.B. Xiao, and Q. Feng, Quantitative Microstructural Evolution and Corresponding Stress Rupture Property of K465 Superalloy, *Mater. Sci. Eng. A*, 2016, **651**, p 734–744
8. Z.H. Gao, P. Zhang, J. Li, J. Yan, and X.F. Gong, Microtwinning in Ni-Base Superalloy Mar-M247 at Intermediate Temperature And Low Stress, *Mater. Lett.*, 2021, **289**, p 129426
9. A.M.S. Costa, E. Hawk, J. Dansbury, and C.A. Nunes, Creep Properties of Directionally Solidified Nb-Modified Ni-Base Superalloy, Mar-M247, *J. Mater. Eng. Perform.*, 2018, **27**, p 5744–5751
10. G.D. Zhao, X.M. Zang, and W.R. Sun, Role of Carbon in Modifying Solidification and Microstructure of a Ni-Based Superalloy with High Al and Ti Contents, *J. Iron Steel Res. Int.*, 2020, **28**, p 98–110
11. Q. Hu, L. Liu, X.B. Zhao, S.F. Gao, J. Zhang, and H.Z. Fu, Effect of Carbon and Boron Additions on Segregation Behavior of Directionally Solidified Nickel-Base Superalloys with Rhenium, *Trans. Nonferrous Met. Soc. China*, 2013, **23**, p 3257–3264
12. L.R. Liu, T. Jin, N.R. Zhao, Z.H. Wang, X.F. Sun, H.R. Guan, and Z.Q. Hu, Effect of Carbon Additions on the Microstructure in a Ni-Base Single Crystal Superalloy, *Mater. Lett.*, 2004, **58**, p 2290–2294
13. K.A. Al-Jarba and G.E. Fuchs, Effect of Carbon Additions on the As-Cast Microstructure and Defect Formation of a Single Crystal Ni-Based Superalloy, *Mater. Sci. Eng. A*, 2004, **373**, p 255–267
14. A.J. Wasson and G.E. Fuchs, Microstructural Evolution of a Carbon Modified Single Crystal Ni-Base Superalloy, *Mater. Charact.*, 2012, **74**, p 11–16
15. J. Picha, Microstructural and Phase Equilibria Study in the Ni–Al–Cr–W System at 1173 and 1273 K, *Intermetallics*, 2003, **11**, p 483–490
16. K.M. Imran, A.O. Mostafa, A. Mohammad, E. Elhachmi, and M. Mamoun, Influence of Cooling Rate on Microsegregation Behavior of Magnesium Alloys, *J. Mater. Sci. Technol.*, 2014, **2014**, p 18
17. R. Be Njamen, M. Carla, M.R. Lais, L.G. Inmaculada, B. Marion, and T. Werner, Effect of Porosity and Eutectics on the High-Temperature Low-Cycle Fatigue Performance of a Nickel-Base Single-Crystal Superalloy, *Scr. Mater.*, 2018, **155**, p 139–143
18. Q.Z. Chen, Y.H. Kong, C.N. Jones, and D.M. Knowles, Porosity Reduction by Minor Additions in RR2086 Superalloy, *Scr. Mater.*, 2004, **51**, p 155–160
19. X.W. Li, T. Liu, L. Wang, X.G. Liu, L.H. Lou, and J. Zhang, Effect of Carbon Content on the Microstructure and Creep Properties of a 3rd

- Generation Single Crystal Nickel-Base Superalloy, *Mater. Sci. Eng. A*, 2015, **639**, p 732–738
20. Y.Z. Liang, A. Li, X. Cheng, X.T. Pang, and H.M. Wang, Prediction of Primary Dendritic Arm Spacing During Laser Rapid Directional Solidification of Single-Crystal Nickel-Base Superalloys, *J. Alloys Compd.*, 2016, **688**, p 133–142
 21. F.D. Geuser and B. Gault, Metrology of Small Particles and Solute Clusters by Atom Probe Tomography, *Acta Mater.*, 2020, **188**, p 406–415
 22. L.G. Min, L.Q. Chi, and J.Z. Cui, Thermodynamic Properties of Binary Alloys of Zn-Mn and Zn-Ti, *Acta Metall. Sin.*, 2001, **11**, p 1004–1609
 23. Q. Li, J. Xie, J.J. Yu, D. Shu, and Y. Zhou, Solidification Behavior and Segregation Characteristics of High W-content cast Ni-Based Superalloy K416B, *J. Alloys Compd.*, 2020, **854**, p 156027
 24. B. Lawrence, C.W. Sinclair, and M. Perez, Carbon Diffusion in Supersaturated Ferrite: A Comparison of Mean-Field and Atomistic Predictions, *Model. Simul. Mater. Sci. Eng.*, 2014, **22**, p 065003
 25. J.H. Chen, C.Y. Lee, and S.J. Jo, MC Carbide Formation in Directionally Solidified MAR-M247 LC Superalloy, *Mater. Sci. Eng. A*, 1998, **247**, p 113–125
 26. X.W. Li, L. Wang, J.S. Dong, and L.H. Lou, Effect of Solidification Condition and Carbon Content on the Morphology of MC Carbide in Directionally Solidified Nickel-Base Superalloys, *J. Mater. Sci. Technol.*, 2014, **30**, p 1296–1300
 27. Y.R. Zheng, L. Zheng, Q. Zeng, and Z.C. Ruan, Formation of Primary M_6C Carbide and Its Effect on Cast Die Superalloys with High Content of Tungsten, *Acta Metall. Sin.*, 2004, **40**, p 285–290
 28. M. Zhong, H. Sun, W. Liu, X. Zhu, and J. He, Boundary Liquation and Interface Cracking Characterization in Laser Deposition of Inconel 738 on Directionally Solidified Ni-Based Superalloy, *Scr. Mater.*, 2005, **53**, p 159–164
 29. Q.Z. Chen, C.N. Jones, and D.M. Knowles, The Grain Boundary Microstructures of the Base and Modified RR 2072 Bicrystal Superalloys and Their Effects on the Creep Properties, *Mater. Sci. Eng. A*, 2004, **385**, p 402–418

Publisher's Note Springer Nature remains neutral with regard to jurisdictional claims in published maps and institutional affiliations.